PNAS RESEARCH ARTICLE | CHEMISTRY OPEN ACCESS

Chirality enhances oxygen reduction

Yutao Sang[a], Francesco Tassinari[a,b], Kakali Santra[a], Wenyan Zhang[a], Claudio Fontanesi[b], Brian P. Bloom[c], David H. Waldeck[c], Jonas Fransson[d], and Ron Naaman[a,1]

Edited by Paul Weiss, University of California, Los Angeles, CA; received February 13, 2022; accepted June 7, 2022 by Editorial Board Member Stephen J. Benkovic

Controlled reduction of oxygen is important for developing clean energy technologies, such as fuel cells, and is vital to the existence of aerobic organisms. The process starts with oxygen in a triplet ground state and ends with products that are all in singlet states. Hence, spin constraints in the oxygen reduction must be considered. Here, we show that the electron transfer efficiency from chiral electrodes to oxygen (oxygen reduction reaction) is enhanced over that from achiral electrodes. We demonstrate lower overpotentials and higher current densities for chiral catalysts versus achiral ones. This finding holds even for electrodes composed of heavy metals with large spin–orbit coupling. The effect results from the spin selectivity conferred on the electron current by the chiral assemblies, the chiral-induced spin selectivity effect.

oxygen | respiration | fuel cells | chirality | spin

Significance

The oxygen reduction reaction is essential to aerobic respiration and is a fundamental chemical reaction in fuel cells. The reaction converts triplet oxygen to products that are all in singlet electronic states, and its understanding requires spin considerations. We show that the oxygen reduction can be enhanced by controlling the spin of the electrons transmitted to the oxygen. We achieve this control by using a chiral electrode and the chiral-induced spin selectivity effect to direct the reaction efficiently on a triplet potential energy surface. This mechanistic feature may help explain the efficiency of respiration in living organisms, which contain chiral enzymes, and provides a strategy for improving catalyst efficiency in fuel cells.

Controlled oxygen reduction reaction (ORR) (1–3) is central for aerobic life (4) and for developing clean energy technologies like fuel cells (5, 6). Understanding the detailed mechanism of the ORR is challenging because one must consider spin selection rules; the ground electronic state of diatomic oxygen is a triplet ($^3\Sigma_g^-$), while the reaction products are in closed-shell singlet states. Indeed, current fuel cell technologies use rare metal catalysts, which possess significant spin–orbit coupling. In contrast, aerobic organisms perform the ORR without needing precious metals. One might ask how the oxidation of glucose to water and CO_2, a complex multistep reaction involving six O_2 molecules, occurs so efficiently in nature. Indeed, this question has been investigated, and detailed mechanisms have been proposed (7). While some enzymes possess metal cofactors with significant spin–orbit couplings that may relax spin constraints in the reaction (8), enzymes without metal cofactors are known to facilitate the efficient reduction of oxygen as well (9, 10). It seems clear that important subtleties of the biochemical mechanism remain elusive (11).

Despite a very substantial effort, the intrinsic electroactivity of ORR catalysts has improved only slowly (1). The best ORR catalysts are platinum-based, and the adsorption of oxygen on the catalyst is very efficient at low reduction potentials so that the proton and electron transfer are inefficient. Only at high reduction potentials can the reaction proceed due to the decreased stability of the adsorbed oxygen (12, 13). This has been considered as the origin of the observed ORR overpotential and a crucial bottleneck in catalyst development.

Many biomolecules, like proteins and DNA, are chiral. The "conventional wisdom" is that chirality serves as a structural motif to place chemical functionalities in defined positions and orientations that enable biologically relevant functions (14, 15). In the last two decades, however, it has been established that chiral molecules/structures have the special electronic property of preferentially transmitting electrons with one spin direction, called the chiral-induced spin selectivity (CISS) effect (16). As an electron propagates along a molecule's chiral axis, its spin angular momentum can be either pointing parallel or antiparallel to the electron's velocity. Which direction of spin is preferred depends on the handedness of the molecule.

We hypothesize that the multielectron reduction of diatomic oxygen (ORR) is enhanced by using spin polarized electrons and that chiral biomolecules, which are known to spin polarize electrons via the CISS effect, can be used to enhance the ORR efficiency. Previous work demonstrates that electron transport through proteins is spin-dependent (17), including proteins involved in respiration (18). In part, this hypothesis is substantiated by recent reports that the efficiency and selectivity of the oxygen evolution reaction (i.e., anodic oxidation of water to O_2) are enhanced by using chiral anodes or anodes modified with chiral molecules (19, 20).

To test this hypothesis, we examine the electrochemical ORR at electrodes modified with chiral organic monolayers. To further relate our findings to fuel cell technology,

Author affiliations: [a]Department of Chemical and Biological Physics, Weizmann Institute of Science, Rehovot 76100, Israel; [b]Department of Engineering "Enzo Ferrari," University of Modena and Reggio Emilia, 41125 Modena, Italy; [c]Chemistry Department, University of Pittsburgh, Pittsburgh, PA 15260; and [d]Department of Physics and Astronomy, Uppsala University, SE-751 21 Uppsala, Sweden

Author contributions: F.T. and R.N. designed research; Y.S., F.T., K.S., W.Z., C.F., and B.P.B. performed research; Y.S., F.T., B.P.B., D.H.W., J.F., and R.N. analyzed data; and B.P.B., D.H.W., J.F., and R.N. wrote the paper.

The authors declare no competing interest.

This article is a PNAS Direct Submission. P.W. is a guest editor invited by the Editorial Board.

Copyright © 2022 the Author(s). Published by PNAS. This open access article is distributed under Creative Commons Attribution-NonCommercial-NoDerivatives License 4.0 (CC BY-NC-ND).

[1]To whom correspondence may be addressed. Email: ron.naaman@weizmann.ac.il.

This article contains supporting information online at http://www.pnas.org/lookup/suppl/doi:10.1073/pnas.2202650119/-/DCSupplemental.

Published July 18, 2022.

Downloaded from https://www.pnas.org by Uppsala Universitetsbibliotek on August 26, 2022 from IP address 130.238.189.191.

the second part of this work studies the effect of chirality on gold and platinum nanoparticles (NPs). In each case, the ORR performance of the chiral electrodes, particularly the onset potential and the current densities, are compared to their achiral analogs. Platinum NPs were specifically chosen because Pt is the preferred catalyst in fuel cells (21).

Results

We used an electrochemical assay in which O_2 was bubbled into an electrochemical cell, and the reductive current was monitored (Fig. 1*A*). The electrochemical cell was assembled with a Pt counterelectrode, an Ag/AgCl reference electrode, and a working electrode that could be either chiral or achiral. In the first stage of the work, we utilized a 100-nm-thick gold film that was coated with a self-assembled monolayer (SAM) of enantiopure chiral cysteine and oligopeptides, SH-$(CH_2)_2$-NH-(Ala-Aib)$_n$-COOH (n = 3, 5, 7, 8, 11, referred to as L-ala3, L-ala5, L-ala7, L-ala8, and L-ala11, respectively) or with a monolayer of achiral alkanethiol molecules, SH-$(CH_2)_n$-CH_3 (n = 3, 7, 9, 13, 17) (*SI Appendix*, Table S1). Note that self-assembled films of these molecules have been extensively characterized by us and others (22, 23). To ensure that the particular monolayers used here were well-formed, the monolayer formation was characterized by infrared spectroscopy, using polarization modulation-infrared reflectance-absorption spectrometry (PM-IRRAS; *SI Appendix*, Figs. S1–S3). The electrochemical reduction was performed at pH = 13 in 0.1 M KOH aqueous solution. Oxygen was bubbled for at least 30 min before starting the measurements to ensure saturation. All applied potentials were converted to the standard reversible hydrogen electrode (RHE) reference scale.

Under the alkaline conditions of these studies, two reduction pathways are commonly considered to be possible (24):

$$O_2 + 2H_2O + 4e^- \rightarrow 4OH^- \quad [1]$$

$$O_2 + H_2O + 2e^- \rightarrow HO_2^- + OH^-$$
$$HO_2^- + H_2O + 2e^- \rightarrow 3OH^-. \quad [2]$$

Fig. 1*B* presents current versus potential curves (linear sweep voltammetry) for electrodes that are coated with a SAM of achiral 3-mercaptopropionic acid (blue) or with chiral L-cysteine (red). The infrared intensities of the characteristic peaks for both L-cysteine and 3-mercaptopropionic acid are almost identical and indicate a similar surface coverage (*SI Appendix*, Fig. S1). The substantial difference of current density in O_2 and N_2 saturated solutions indicates that both chiral- and achiral-functionalized electrodes show activity for oxygen reduction (Fig. 1*B* and *SI Appendix*, Fig. S4). Despite the two molecules' being of the same length and of very similar structure (Fig. 1*B*), a shift of about 0.17 V in the onset potential for the reduction is clearly evident. The onset potential is defined as the potential at which the current reaches a value of 0.1 mA/cm^2 (black dotted line in Figs. 1*B* and 2 *A* and *B*). Please note that a more positive potential corresponds to a lower barrier for the ORR (25). Because these data support the initial hypothesis, more extensive and detailed studies with the proper control experiments were performed.

Because chiral SAMs are known to spin-polarize electron currents, whereas achiral SAMs do not, we compared the ORR for achiral and chiral molecule coatings to assess the effect of spin polarization. Fig. 2 presents the linear sweep voltammograms for the ORR when the working electrode is coated with achiral (Fig. 2*A*) and chiral molecules (Fig. 2*B*) of different lengths. The results for the achiral carboxylic acids, which possess a hydrophilic carboxylic tail group, are shown in *SI Appendix*, Fig. S5. As shown by Fig. 2*C*, the onset potential becomes more negative with increasing molecular length for the achiral molecules, independent of whether they possess a methyl (CH_3) or carboxylic (COOH) tail functional group. In contrast, the onset potential becomes more positive with increasing molecular length for the chiral molecules, indicating a decrease in the onset potential with increasing SAM thickness. To confirm that the onset potential shift does not arise from significant differences in the potential drop through the SAM layer, or SAM quality, with length, cyclic voltammograms were measured for the ferri/ferrocyanide [$Fe(CN)_6^{3-/4-}$] redox couple instead of oxygen (*SI Appendix*, Fig. S6). Because achiral ferricyanide is a low-spin d^5 complex and ferrocyanide is a low-spin d^6 coordination complex, no effect from spin polarization is expected for this redox couple. For the $Fe(CN)_6^{3-/4-}$, the surfaces coated with shorter molecules show a much higher redox peak current than that of longer molecules, independent of whether the molecules are chiral or achiral; however, the apparent redox potential of the $Fe(CN)_6^{3-/4-}$ does not change

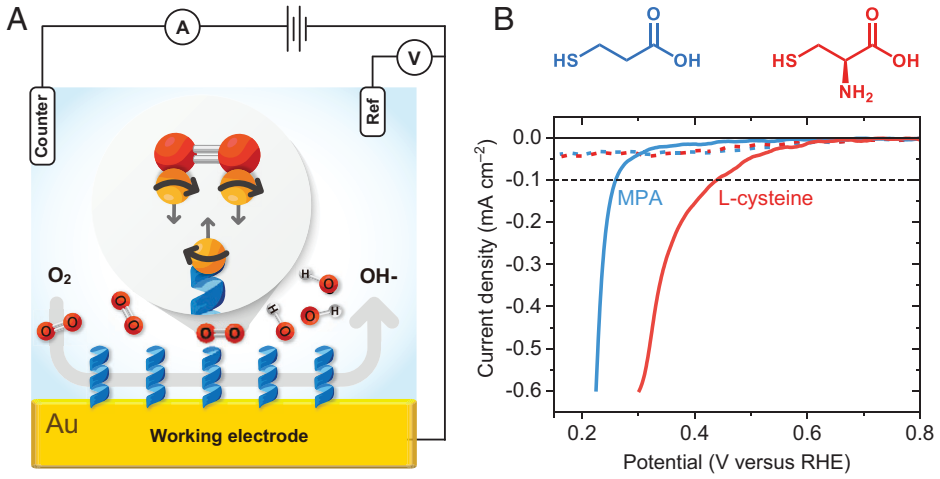

Fig. 1. The experimental setup and the effect of chiral monolayers on oxygen reduction. (*A*) A schematic layout of the electrochemical setup, which includes a gold working electrode coated with a SAM of either chiral or achiral molecules. The potentials reported here were converted to the standard RHE reference scale. Note that the working electrode was static during these measurements. (*B*) As a demonstration, the linear sweep voltammogram that was measured when the electrode was coated with a monolayer of achiral molecules (3-mercaptopropionic acid, blue curves) or with chiral molecules (L-cysteine, red curves) in N_2 (dashed) and O_2 (solid)-saturated 0.1 M KOH aqueous solution. The onset potential is defined as the potential when the current reaches 0.1 mA/cm^2, as shown by the dotted black line. Current densities were normalized in reference to the geometric area of the working electrode.

Downloaded from https://www.pnas.org by Uppsala Universitetsbibliotek on August 26, 2022 from IP address 130.238.189.191.

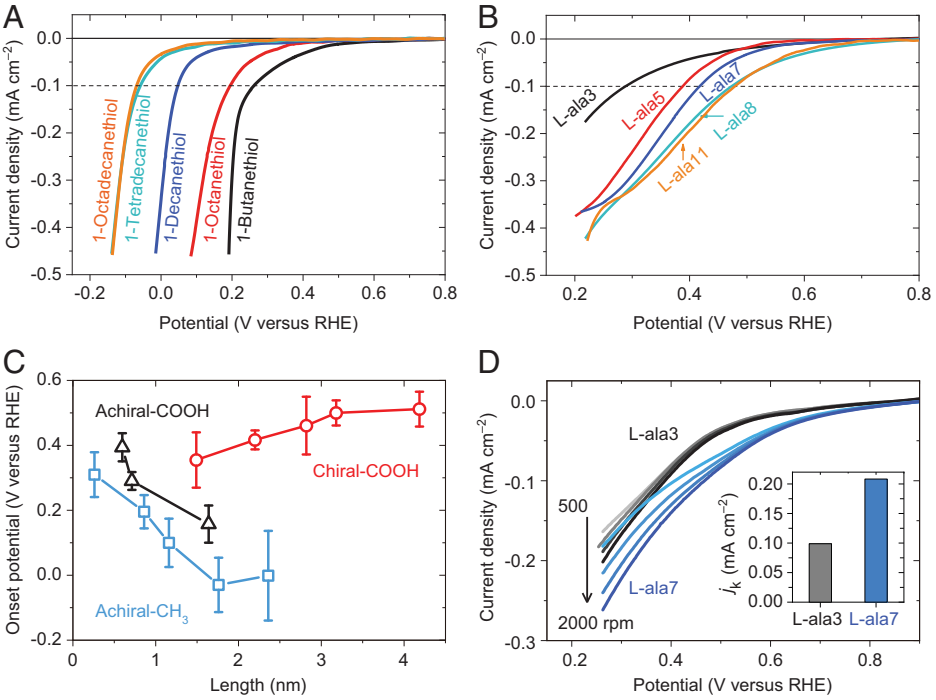

Fig. 2. The molecular length-dependent oxygen reduction. The ORR polarization curves of (*A*) achiral and (*B*) chiral monolayers of various molecular lengths in O_2-saturated 0.1 M KOH at room temperature and a potential scan rate of 50 mV/s. (*C*) The onset potentials (at 0.1 mA·cm^{-2}) versus molecular length for working electrodes modified with monolayers of different lengths. For chiral monolayers, the onset potential becomes more positive as the length increases, indicating a lower barrier for reduction. On the contrary, the onset potential of the achiral monolayers become more negative as the molecular length increases, indicating a higher barrier for reduction. Both hydrophobic (achiral-CH_3) and hydrophilic (achiral-COOH) monolayers were studied and revealed a similar behavior as a function of length. (*D*) ORR polarization curves obtained by the RDE method for L-ala7 and L-ala3 in air-saturated 0.1 M KOH at a sweep rate of 5 mV·s^{-1} from 500 rpm to 2,000 rpm. (*Inset*) The kinetic current density (j_k) of L-ala7 and L-ala3 for O_2 reduction at 0.4 V.

significantly with thickness for a given SAM type. These findings are corroborated by impedance measurements which show that the impedance increases with the length for both types of molecules (*SI Appendix*, Table S2 and Fig. S7).

The voltammograms for the peptides (Fig. 2*B*) show a positive shift of the onset potential and a shallower *i-V* slope as compared to the achiral SAMs (Fig. 2*A*). Because the peptide molecules are dipolar, they can impart a potential drop across the SAM. A comparison of the cyclic voltammograms for the SAM coated electrodes with $Fe(CN)_6^{3-/4-}$ (*SI Appendix*, Fig. S6) show a shift of about 200 mV more negative for the peptide-coated electrodes than the achiral electrodes. This observation indicates that the strong positive onset potential shifts arise from a difference in the overpotential for the alkane (achiral) and peptide (chiral) films, with the chiral films displaying the lower overpotential. We posit that the shallower *i-V* slope arises from ORR's being closer to diffusion-limited for the chiral SAMs. The better ORR activity of the chiral monolayer was also gleaned from the smaller Tafel slope than that measured with an achiral monolayer in 0.1 M KOH (*SI Appendix*, Figs. S8 and S9) (26, 27). The achiral monolayers have a higher average Tafel slope than the chiral monolayers (*SI Appendix*, Fig. S8). The observed higher reaction barrier for achiral molecules is consistent with the fact that the increased molecular length of alkanes results in increased electrical resistance and a decreased O_2 solubility (28). Hence, one expects that a lower potential (higher overpotential) will be required to achieve the same current density for a thick film as that observed for a thin film. Surprisingly, though, the onset potential of electrodes comprising chiral molecules increases with the length, even though the molecules' charge transfer resistance is known to increase with length for the ferri/ferrocyanide case, and the diffusion of O_2 through the layer to the electrode is expected to decrease with the molecular length.

The unusual decrease of the ORR reaction barrier with increasing oligopeptide length was further studied by rotating-disk electrode (RDE) measurements for L-ala7 and L-ala3 (see *Materials and Methods* and Fig. 2*D*). To avoid desorbing the monolayer, the potential scan was stopped at 0.25 V (versus RHE) and the plateau (diffusion-limiting) current was not reached. Although both SAMs show an increase in the current with increasing rotation speed, the current density of L-ala7 is always higher than that of L-ala3 at the same rotation speed. Both the L-ala7 and L-ala3 SAMs show linear and nearly parallel Koutecký–Levich plots (J^{-1} versus $\omega^{-1/2}$) (*SI Appendix*, Fig. S9 *A* and *B*) (26) and plots of overpotential versus log of current density (*SI Appendix*, Fig. S9 *C* and *D*) show that the kinetic current (j_k) of L-ala7 is always higher than that of L-ala3 at a given overpotential. Other kinetic descriptors of the catalytic activity are consistent with this finding (see the analysis in *Materials and Methods* and *SI Appendix*, Fig. S9). We attribute the enhanced ORR activity of the longer L-ala7 to the improved spin filtering of oligopeptides with increasing length (see below) (22).

Despite the clear differences in the ORR reaction between chiral and achiral monolayer coated electrodes, one must ask whether these differences arise from the chiral symmetry and spin filtering or whether they arise from the different chemical properties of the alkane and peptide molecules. Moreover, does the chirality enhancement hold for architectures that more closely mimic that found for state-of-the-art applications? To address these questions, experiments were performed with electrocatalysts, Au NPs and Pt NPs, that differ by their chiral symmetry but possess the same composition. The use of nanoparticles affords chiral imprinting onto the particle density of states which ought to further increase the spin polarization, discussed below, as well as a larger surface area which is conducive to a higher catalytic activity over planar coated electrodes.

Downloaded from https://www.pnas.org by Uppsala Universitetsbibliotek on August 26, 2022 from IP address 130.238.189.191.

We synthesized Au NPs in the presence of cysteine (see *Materials and Methods* for more details). The chiral symmetry of the Au NPs is controlled by the enantiomeric form of the cysteine and was confirmed by circular dichroism (CD) spectroscopy (*SI Appendix*, Fig. S10). The ORR onset potential obtained with the chiral Au NPs was 178 mV higher than that of the Au NPs made with a racemic mixture of cysteine (Fig. 3*A*). Considering the large spin–orbit coupling of gold, the increased ORR onset potential confirms the additional contribution of the spin-polarized electrons induced by the chiral molecules. As will be shown below, this contribution must go beyond only relaxing the spin selection rules.

To probe the effect of chirality on materials used in fuel cells, we examined the performance of platinum—the archetypal electrocatalyst for oxygen reduction (29–32). Chiral Pt NPs were synthesized in the presence of L-cysteine, and achiral Pt NPs were made with a racemic mixture of L- and D-cysteine in the synthesis (*SI Appendix*, Fig. S11). The L-cysteine–modified NPs show clear CD signals in the absorption spectrum region of the NPs, whereas the racemic cysteine-modified NPs are CD-silent (*SI Appendix*, Fig. S12). The performance of the ORR was evaluated using the RDE method, and measurements on a commercial Pt/C (nominally 20% Pt on carbon black) catalyst were also conducted as a benchmark. Fig. 3*B* shows the ORR polarization curves in air-saturated 0.1 M KOH solution. The chiral Pt NPs have an onset potential of 0.92 V at -0.1 mA·cm^{-2} (Fig. 3*C*), which is modestly higher (30 mV) than that found for the commercial Pt/C and significantly higher (80 mV) than the achiral Pt NPs. Moreover, chiral Pt NPs also exhibit a higher half-wave potential (0.87 V) than that of achiral NPs (0.80 V) and Pt/C (0.84 V). We then studied the Tafel plots (33) from the ORR polarization curves at 1,500 rpm, and the results are shown in *SI Appendix*, Fig. S13. The smaller Tafel slope obtained for chiral Pt NPs, as compared with Pt/C and achiral NPs, demonstrates its faster ORR kinetics. These results indicate that chirality enhances the ORR reaction rate, even in the case of electrodes with high spin–orbit coupling.

To further quantify the intrinsic ORR activity, the kinetic current of each catalyst was obtained using the Koutecký–Levich equation (see *Materials and Methods*), and then the mass activity and specific activity at the commonly chosen value of 0.9 V versus RHE (30) were compared (Fig. 3*D*). The mass activity of chiral Pt NPs is 2.7 and 48.5 times higher than that of commercial Pt/C and achiral Pt NPs catalysts, respectively. Here, the electrochemically active surface area (ECSA) (*SI Appendix*, Fig. S14) was used for determining the specific activity, and the chiral Pt catalyst was found to be 8.5 and 40.3 times higher than that of commercial Pt/C and achiral Pt NPs, respectively.

Previous studies have shown that the coupling of the electron spin direction to the molecule's chiral axis exceeds the thermal energy significantly at room temperature (34) and that chiral molecules serve as spin filters (35). A measure for the spin-dependent filtering is provided by the spin polarization P, which is defined as

$$P = \frac{I_\alpha - I_\beta}{I_\alpha + I_\beta}, \qquad [3]$$

where I_α is the electron current with the electron spins pointing parallel to their velocity and I_β is the electron current with their spin pointing antiparallel to their velocity. The effect of chiral molecules on the ORR efficiency can be revealed by probing the correlation between the length of the chiral molecules and the spin

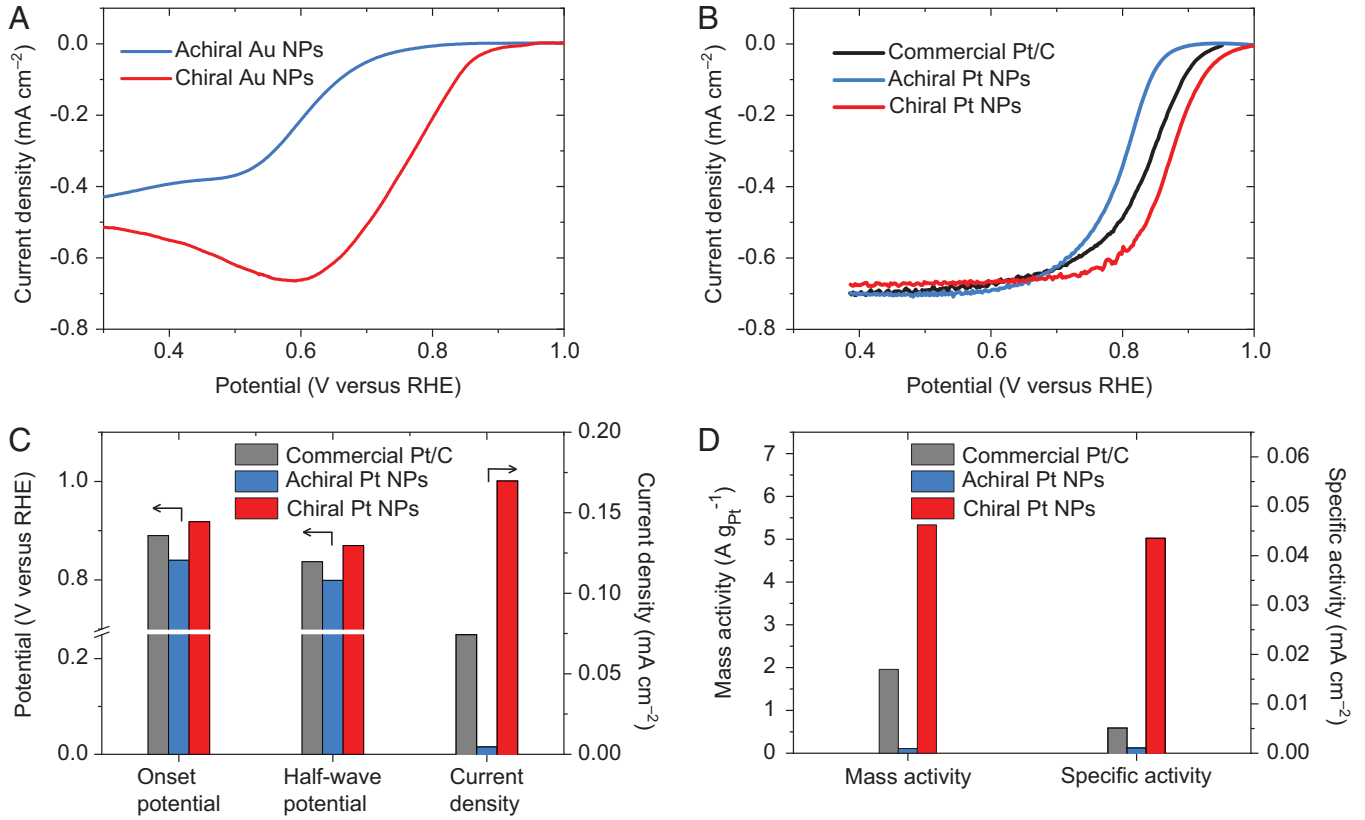

Fig. 3. Chirality enhances ORR activities of inorganic NPs. (*A*) The static ORR polarization curves were measured with chiral and achiral Au NPs in O_2-saturated 0.1 M KOH solution at a sweep rate of 50 mV/s. (*B*) RDE measurements of the ORR polarization curves of chiral and achiral Pt NPs and the commercial catalysts Pt/C in air-saturated 0.1 M KOH at 1,500 rpm and a sweep rate of 5 mV·s^{-1}. (*C*) Comparisons of onset potentials (identified as the potential at -0.1 mA·cm^{-2}), half-wave potentials ($E_{1/2}$), and current density at 0.9 V (versus RHE, right scale). (*D*) A comparison of mass activity and specific activity at 0.9 V versus RHE.

Downloaded from https://www.pnas.org by Uppsala Universitetsbibliotek on August 26, 2022 from IP address 130.238.189.191.

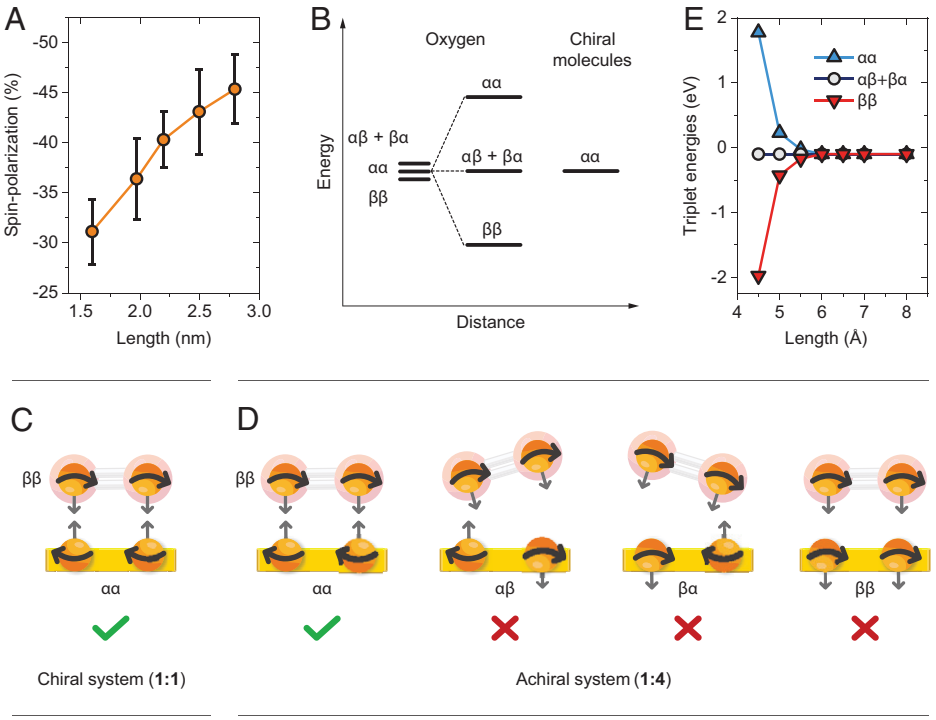

Fig. 4. The effect of chiral molecules. (*A*) The dependence of the spin polarization on the length of chiral oligopeptides, adapted with permission from ref. 22. (*B*) The splitting in the spin states of the triplet oxygen upon interaction with the spin-polarized electrons residing on the chiral molecules. The possible spin states in the case of (*C*) a chiral system and in the case of (*D*) an achiral one. In the case of an achiral system the two electrons can have four possible configurations from which only one of them leads to reaction. There is only one possible configuration in the chiral system, and the electrons are strongly coupled to the molecular frame. As a result, this is the only configuration that can lead to the reaction. (*E*) The calculated triplet energy levels on the oxygen presented as a function of the distance between the chiral molecule and the oxygen. The Zeeman splitting, which causes the stabilization of one triplet state on the oxygen, is about 100 meV (5 kT at room temperature) at a distance of 0.55 nm between the interacting electrons.

polarization of the electrons transmitted through them. As reported earlier, the L-oligopeptides used here (Fig. 4*A*) select for spins aligned parallel to the electron velocity and the magnitude of the spin polarization increases from 30 to 45% as the oligopeptide length increases (22).

Discussion

How does the spin polarization of the electron current affect the reduction of oxygen? Independent of the exact mechanism of the oxygen reduction, it requires at least two electrons in the first stage to generate either O_2^{2-} or HO_2^- (24). In considering the spin statistics, it is the projection of the O_2 molecule's spin onto the chiral axis emanating from the molecular layer that is important as an O_2 molecule approaches the electrode. For O_2, with its unpaired electrons, 1 and 2, three possible spin states, $\alpha(1)\alpha(2)$, $\beta(1)\beta(2)$, and $[\alpha(1)\beta(2) + \beta(1)\alpha(2)]/\sqrt{2}$, are possible. In the case of chiral oligopeptides, the two electrons injected from the monolayer have the same spin projection on the molecular axis, namely, their state will be $\alpha\alpha$ (Fig. 4*B*). Thus, the reaction barrier is affected by an entropic factor (related to the spin statistics) and an enthalpic factor arising from the stabilization of the $\beta(1)\beta(2)$ state of the O_2 by the spin-exchange interaction with the polarized electrons on the chiral molecules.

Fig. 4 *B*–*D* illustrate the spin polarization effect. While in the chiral molecules, the spin direction is defined with respect to the molecular axis, the three degenerate spin states on the oxygen split as the molecule approaches the chiral monolayers; i.e., its spin states split, like in the case of a magnetic field, and the state $\beta(1)\beta(2)$ will be stabilized. As the oxygen interacts (the electron clouds overlap) with the chiral monolayer film, these interactions grow in strength because of the spin-exchange effect (Fig. 4*B*). This effect reduces the enthalpic barrier, and a more efficient injection of the spins from the monolayer into the oxygen system results. Moreover, the O_2's spin-state alignment with the chiral film reduces the entropic contributions to the free energy barrier (Fig. 4 *C* and *D*). For the achiral film, there are four spin states possible in the monolayer, $\alpha\alpha$, $\beta\beta$, $\alpha\beta$, and $\beta\alpha$, from which only one will enable efficient electron transfer to the oxygen (thus the reaction probability is only one in four). Moreover, because the spins on the achiral monolayers are not coupled to the molecular frame, they will not split the spin states of the oxygen, and the enthalpic barrier will not be reduced.

Model calculations support the mechanism described above. The theoretical simulations treat the chiral molecule as a chain of nuclear sites, each of which carries a single electron level and is coupled to both its nearest neighbors and next-nearest neighbors via both elastic and inelastic spin–orbit interactions (see *Materials and Methods* for more details) (36, 37). Fig. 4*E* shows the effect of the helix's interaction on the energies of the O_2 molecule's spin substates. Although a simple model, the calculations show a splitting of the triplet state sublevels that can be hundreds of millielectronvolts (tens of kilocalories per mole). These findings are consistent with recent works that show enhanced oxygen reduction efficiency with magnetic electrodes (38, 39), presumably because of the spin alignment of the injected electrons. Because the calculations are based on a model that involves a significant approximation, the splitting energies given in Fig. 4*E* should not be considered precise, but rather as providing the right order of magnitude.

Using this model for the spin-dependent reaction, it is possible to estimate the enhancement in the reaction rate that manifests with chiral electrodes. We assume that the difference in

Downloaded from https://www.pnas.org by Uppsala Universitetsbibliotek on August 26, 2022 from IP address 130.238.189.191.

activation entropy for the chiral and achiral cases arises from the difference in the number of possible spin arrangements and that the difference in activation enthalpy arises from the difference in Zeeman energy. With an achiral film, the activation entropy, $\Delta S^{\ddagger}$, that is associated with the spin state is $-k$ ln3 (because 1 of 3 triplets is aligned correctly), and the activation enthalpy, $\Delta H^{\ddagger}$, has a net zero Zeeman stabilization. With a chiral film, the activation entropy $\Delta S^{\ddagger}$ from the spin is 0, and the activation enthalpy has a Zeeman stabilization of $\varepsilon \sim \Delta H^{\ddagger}$. If the Zeeman stabilization is −100 meV, the chiral system has

$$\begin{aligned}\Delta G^{\ddagger}_{chiral} &= \Delta H^{\ddagger} - T \cdot \Delta S^{\ddagger} \\ &= \left(\Delta H^{\ddagger}_{no\ spin} - 0.1\ \text{eV}\right) - (298) \cdot \left(\Delta S^{\ddagger}_{no\ spin} + k\ln(0)\right) \\ &= \Delta H^{\ddagger}_{no\ spin} - 0.1\ \text{eV},\end{aligned}$$

and the achiral system has

$$\begin{aligned}\Delta G^{\ddagger}_{achiral} &= \Delta H^{\ddagger} - T \cdot \Delta S^{\ddagger} \\ &= \left(\Delta H^{\ddagger}_{no\ spin} - 0\right) - (298) \cdot \left(\Delta S^{\ddagger}_{no\ spin} - k\ln(3)\right) \\ &= \Delta H^{\ddagger}_{no\ spin} + 0.028\ \text{eV}.\end{aligned}$$

Thus, we have a $\Delta(\Delta G^{\ddagger}.) = \Delta G^{\ddagger}_{chiral} - \Delta G^{\ddagger}_{achiral} = -0.128$ eV, which would imply an enhancement in the rate constant of 146 times. If instead the Zeeman stabilization is only 25 meV (i.e., ∼kT), then we find $\Delta(\Delta G^{\ddagger}.) = -0.056$ eV and a rate enhancement of 8.9 times. If the Zeeman stabilization is neglected, then $\Delta(\Delta G^{\ddagger}.) = -0.028$ eV, which gives an enhancement of the rate by about three times.

Although the proposed mechanism considers simultaneous two-electron reduction, this analysis is appropriate for a sequential process, as long as the second electron is injected on a time scale shorter than the spin depolarization time.

Given that the CISS effect can enhance the rate of multielectron reaction steps by reducing the number of accessible spin channels, it is interesting to conjecture about its implications for the glucose oxidation process, which involves 6 oxygen molecules and 24 electrons. With a large number of multielectron transfer steps possible in such a complex redox scheme, the reduction in the entropy of activation by spin filtering could enhance the overall rate by more than an order of magnitude for chiral biomolecules. Homochirality in biological organisms represents an entropy reduction that increases the Gibbs free energy of the organisms. It may be that the respiration process and its substantial benefit from homochirality, because of the lower number of possible spin states (lower entropic reaction barrier), helps drive this selection. This mechanism in which spin-filtered electrons enhance the overall reaction efficiency may explain, in part, why life has preserved chirality so consistently over evolution.

The present work demonstrates that controlling the spin in multielectron transfer processes, like the ORR, results in two contributions to the reaction rates. The first is the correspondence with spin selection constraints, allowing for reactions to occur on a triplet potential energy surface. The second is in reducing the number of states available for the reactions, thereby reducing entropic barriers. The present results imply that control over the electron spin is an important attribute for catalysts used in oxygen-related reactions, and it reduces the overpotential and increases the current density.

Materials and Methods

Monolayer Formation. The solutions used to prepare the monolayer were first bubbled with Ar for more than 30 min. The achiral alkanethiol molecules were dissolved in ethanol to form a 1 mM solution. The chiral oligopeptides were dissolved in 2,2,2-trifluoroethanol (≥99%; Sigma-Aldrich) to form a transparent solution of 1 mM. The Au film electrodes were prepared by e-beam evaporation on single-crystal silicon wafers with a combination of Cr (10 nm)/Au (100 nm) layers. Prior to adsorption, the surfaces were cleaned by boiling in acetone and in ethanol for 10 min each, followed by ultraviolet/ozone treatment for 15 min, and then immersed in ethanol for 40 min. These surfaces were then dried under nitrogen gas flow and immediately immersed in the solution of thiol molecules for 72 h.

PM-IRRAS. PM-IRRAS was used to characterize the chiral and achiral monolayers on the gold electrodes. The spectra were recorded using a Nicolet 6700 Fourier transform infrared instrument equipped with a PEM-90 photoelastic modulator (Hinds Instruments). Each spectrum was obtained by accumulating 2,000 scans with the samples mounted at a Brewster angle of 80°. The spectra are shown in *SI Appendix*, Figs. S1–S3.

Synthesis of Chiral Gold NPs. The synthesis of chiral gold NPs was done by following the procedure reported in ref. 40. Typically, cubic Au seeds were first synthesized and dispersed in an aqueous cetyl trimethyl ammonium bromide (CTAB) (1 mM) solution; 0.8 mL of 100 mM CTAB and 0.2 mL of 10 mM gold chloride trihydrate were added into 3.95 mL of deionized water as the growth solution. Cubic seed solution was then added to the growth solution, and 100 μM cysteine was added after 20 min. The sample was placed in a 30 °C bath for 2 h, and the pink solution gradually became blue with a large scattering. The solution was centrifuged twice to remove unreacted reagents.

Synthesis of Chiral Platinum NPs. Pt NPs were synthesized using chloroplatinic acid hydrate and L- or DL-cysteine as ligands with water as a reaction media. In 718 μL of E-pure water, 82 μL of 122 mM chloroplatinic acid, 200 μL of 7.5 mM L- or DL-cysteine, and 200 μL of 200 mM $NaBH_4$ were added. For the CD measurements, the concentration of cysteine was increased to 50 mM. After 2 h of magnetic stirring in a N_2 atmosphere at room temperature, brownish transparent NP dispersions were obtained. After sufficient purifications, the synthesized NPs were analyzed by rinsing NPs with E-pure water. The precipitation was done by adding a larger volume of isopropanol followed by centrifugation for 20 min at 10,000 rpm.

CD Measurements. The CD measurements were carried out using a Chirascan spectrometer (Applied Photo Physics). The measurement conditions for all spectra were done at a scan range of 185 to 700 nm, 0.5 s time per point, 1-nm step size, and a 1-nm bandwidth. A quartz cuvette with an optical pathway of 2 mm was used for the solution sample.

Electrochemical Tests. Electrochemical measurements were performed using a three-electrode electrochemical cell, equipped with an Ag/AgCl (3 M NaCl) reference electrode and a platinum wire as the counterelectrode. The working electrode was an Au film modified with different molecules (see above). Electrochemical data were recorded at room temperature on a potentiostat (PalmSens4) electrochemical workstation. The potential was measured versus an Ag/AgCl reference electrode and then calibrated with reference to a standard RHE. Note that the working electrode was static during all the measurements.

The electrolyte for ORR was 0.1 M aqueous KOH (pH 13). Before each measurement, the electrolyte was purged with O_2 for 30 min and subjected to O_2 flow during the tests. The operation procedures were the same for the control experiments, except the O_2 was replaced with N_2. The oxygen reduction properties of molecule-coated surfaces were studied at room temperature by using linear sweep voltammetry at a scan rate of 50 mV/s. Cyclic voltammetry (*SI Appendix*, Fig. S6) and electrochemical impedance spectra (*SI Appendix*, Fig. S7) were collected in an aqueous solution with 0.1 M KCl and 10 mM $Fe(CN)_6^{3-/4-}$. Electrochemical impedance spectra were conducted with a frequency range of 50 kHz to 5 Hz.

For the Au and Pt NPs, the same amount of chiral or achiral NPs was dispersed in water by vigorous stirring and sonication. Eight microliters of the NPs solution was dropped onto a glassy carbon electrode (GCE; 3 mm in diameter from ALS Co., Ltd., Japan). The loading amount of metal Pt was kept as 42 μg/cm^2

Downloaded from https://www.pnas.org by Uppsala Universitetsbibliotek on August 26, 2022 from IP address 130.238.189.191.

geometric area (confirmed by inductively coupled plasma mass spectrometry). After water evaporation at room temperature for 3 h, 4 μL of 0.05 wt % Nafion solution was dropped on the electrode surface to cover and stabilize the NP assembly on the electrode surface. Such an NP-loaded GCE was immersed into the solution as a working electrode. ORR activities were measured under oxygen purging in O_2-saturated 0.1 M KOH at room temperature.

The ECSA was measured by using the hydrogen adsorption/desorption method on platinum in alkaline conditions (41). A 0.1 M KOH aqueous solution was first purged with argon, and a continuous stream of argon was introduced into the cell to maintain an inert atmosphere. The cyclic voltammograms were recorded between 0.0 V and 1.2 V versus the RHE with a scan rate of 50 mV/s. The ECSA was determined by integrating the hydrogen adsorption charge on the CVs (*SI Appendix*, Fig. S14), and calculated as ECSA $= Q_{des}/(m \times Q_{ref})$, where Q_{des} is the overall charge of the H desorption, Q_{ref} is the charge density associated with a monolayer adsorption of H_2 on platinum with unit weight, and m is the loading amount of platinum on the electrode.

RDE Measurements and Calculations. The kinetic characterizations of chiral and achiral electrodes for ORR were achieved by using the RDE measurements. The RDE loaded with different catalysts was used as the working electrode. The preparation of RDE electrodes was the same as that for the GCE electrodes. For the SAM-coated electrodes, an Au RDE was used to form the SAM, and the scan range was limited from 0.9 V to 0.25 V (versus RHE) in order to protect the monolayer. The ORR polarization curves were recorded in air-saturated 0.1 M KOH with a sweep rate of 5 mV·s^{-1} at different rotation rates from 500 rpm, 1,000 rpm, and 1,500 rpm to 2,000 rpm.

The recorded RDE curves were iR-corrected before calculating, and several important parameters were determined by Koutecký–Levich equation (26):

$$\frac{1}{j} = \frac{1}{j_{lim}} + \frac{1}{j_k} = \frac{1}{B\omega^{1/2}} + \frac{1}{j_k},$$
$$B = 0.62nFC_0D_0^{2/3}v^{-1/6}$$

where j (A·m^{-2}) is the measured current density, j_{lim} is the measured limiting current density (A·m^{-2}), j_k is the kinetic current densities (A·m^{-2}), ω is the electrode angular rotation rate (rad·s^{-1}), n is the number of electrons transferred, F is the Faraday constant, C_0 is the bulk concentration of O_2 in 0.1 M KOH, υ is the kinetic viscosity of the electrolytes, D_0 is the O_2 diffusion coefficient in 0.1 M KOH, and j^0 is the exchange current density (42). Therefore, B is determined from the slope after fitting the Koutecký–Levich plots, and the electron transfer number (n) can be estimated according to B. In addition, the kinetic currents (j_k) can also be calculated from the intercept of a fit to the Koutecký–Levich plot, and it is proportional to the electron transfer rate constant.

Moreover, since the j_k can be obtained at different electrode potentials, a plot of overpotential (η) versus ln(j_k) has the form (26, 42)

$$\eta = \frac{RT}{(1-\alpha)nF}\ln\left(j^0\right) - \frac{RT}{(1-\alpha)nF}\ln\left(j_k\right),$$

where R is the universal gas constant, T is the absolute temperature, F is the Faraday constant, and α is the electron-transfer coefficient. A best fit by this equation to the data allows us to obtain j^0 from the ratio of the slope and intercept. It should be noted that the calculation of exchange current density from $\eta - \ln(j_k)$ equation is of questionable value for the complicated ORR reaction mechanism (25, 27) and we do not interpret it directly.

Alternatively, the kinetic current I_k may be calculated directly from the Koutecký–Levich equation $Ik = (I_{lim} \times I)/(I_{lim} - I)$, where I_{lim} is the limiting current, and I is the measured current at a given potential. The specific activity and the mass activity were obtained for each catalyst by normalizing the kinetic current to the corresponding ECSA (determined from hydrogen underpotential deposition) and the precious metal loading, respectively.

Model Calculations. The inelastic component in this model is composed of nuclear vibrations that couple to the electronic structure through both spin-independent and spin-dependent electron–vibration coupling. These two components originate from nuclear motion that changes the nuclear confinement potential and, hence, pertains to both the overlap matrix elements included in the tunneling rates between nuclei as well as to the spin–orbit interaction in the structure. The theoretical simulations are performed using a model for the chiral molecule based on a chain of nuclear sites, each of which is carrying a single electron level (ε_m) and is coupled to its nearest neighbors via both elastic (t_0) and inelastic (t_1) hopping and to its next-nearest neighbors via both elastic (λ_0) and inelastic (λ_1) spin–orbit interactions (see refs. 36 and 37). The inelastic component in this model is composed of nuclear vibrations, modes ω_m, that couple to the electronic structure, through both spin-independent (t_1) and spin-dependent (λ_1) electron–vibration coupling. These two components originate from nuclear motion that changes the nuclear confinement potential $V(\boldsymbol{r})$ and, hence, pertain to both the overlap matrix elements included in the tunnelling rates between nuclei as well as to the spin–orbit interaction in the structure (see ref. 36 for more details). The chiral molecule is attached on one end to a metallic reservoir ($\mathcal{H}_{res} = \Sigma_{\boldsymbol{k}}\varepsilon_{\boldsymbol{k}}\psi^{\dagger}_{\boldsymbol{k}}\psi_{\boldsymbol{k}}$) (see refs. 36 and 37), whereas the opposite end is connected to the O_2 molecule via direct exchange interaction v of the form $v = \langle\psi^{\dagger}_N|\boldsymbol{\sigma}\cdot\boldsymbol{S}_{O_2}|\psi_N\rangle$, where $\psi^{\dagger}_N$ (ψ_N) denotes the creation (annihilation) spinor at the molecular site N, whereas $\boldsymbol{\sigma}$ is the vector of Pauli matrices, and $\boldsymbol{S}_{O_2} = \boldsymbol{S}_1 + \boldsymbol{S}_2$ is the spin operator for the O_2 molecule, where $\boldsymbol{S}_{1,2}$ denotes the spin 1/2 operator for the two unpaired electrons. The exchange integral v is calculated as a function of the distance R between the chiral and O_2 molecules by using the expression for the exchange between the electrons in an H_2 molecule (see, e.g., ref. 43):

$$v = j_0\frac{\mathcal{A}-\mathcal{B}}{5a_0},$$
$$\mathcal{A} = \frac{6}{s}\left(S^2(\gamma + \ln s) - S'^2E_1(4s) + 2SS'E_1(2s)\right),$$
$$\mathcal{B} = \left(-\frac{25}{8} + \frac{23s}{4} + 3s^2 + \frac{s^3}{3}\right)e^{-s},\ S = \left(1 + s + \frac{s^2}{3}\right)e^{-s},$$

where $j_0 = e^2/4\pi\varepsilon_0$, e is the electron charge, ε_0 is the vacuum permittivity, $S'(s) = -S(s)$, $s = R/a_0$, a_0 is the Bohr radius, γ is the Euler constant, and $E_1(x)$ is the exponential integral.

For the simulations presented in the main text, we have modeled a chiral molecule with six turns of eight ions per turn, and the parameters (in units of $t_0 = 40$ meV)

where μ is the overall chemical potential for the system, whereas Γ_0 denotes

t_1	λ_0	λ_1	$\varepsilon_m - \mu$	ω_m	Γ_0
1/10	t_0/40	1/100	−2	1/10,000	t_0/1,000

the coupling strength between the metallic reservoir and the chiral molecule. All simulations are done at $T = 300$ K.

One end of the chiral molecule is attached to a metallic reservoir, and the opposite end interacts with the O_2 molecule by a direct exchange interaction v which is calculated as a function of the distance R between the chiral and O_2 molecules (see Fig. 4*E*) by using the expression for the exchange between the electrons in an H_2 molecule (36). The exchange interaction is $v = <\psi^{\dagger}_N|\boldsymbol{\sigma}\cdot\boldsymbol{S}_{O_2}|\psi_N>$, where $\psi^{\dagger}_N$ (ψ_N) denotes the creation (annihilation) spinor at the molecular site N, $\boldsymbol{\sigma}$ is the vector of Pauli matrices, and $\boldsymbol{S}_{O_2}$ is the spin operator for the O_2 molecule. The assembly of the metal, chiral molecule, and O_2 molecule constitutes an open system in which the charge distribution and accompanied spin polarization of the chiral molecule, and the magnetic moment of the O_2 molecule are determined in a self-consistent computation, using nonequilibrium Green functions.

Data Availability. All study data are included in the article and/or *SI Appendix*.

ACKNOWLEDGMENTS. R.N. acknowledges support from the Minerva Foundation. R.N. and D.H.W. acknowledge partial support from US Department of Energy Grant ER46430 and from NSF–Binational Science Foundation grant, CBET 1852588. J.F. acknowledges support from Vetenskapsrådet and Stiftelsen Olle Engkvist Byggmästare.

1. A. Kulkarni, S. Siahrostami, A. Patel, J. K. Nørskov, Understanding catalytic activity trends in the oxygen reduction reaction. *Chem. Rev.* **118**, 2302–2312 (2018).
2. M. Shao, Q. Chang, J. P. Dodelet, R. Chenitz, Recent advances in electrocatalysts for oxygen reduction reaction. *Chem. Rev.* **116**, 3594–3657 (2016).
3. L. Dai, Y. Xue, L. Qu, H. J. Choi, J. B. Baek, Metal-free catalysts for oxygen reduction reaction. *Chem. Rev.* **115**, 4823–4892 (2015).
4. G. T. Babcock, How oxygen is activated and reduced in respiration. *Proc. Natl. Acad. Sci. U.S.A.* **96**, 12971–12973 (1999).

Downloaded from https://www.pnas.org by Uppsala Universitetsbibliotek on August 26, 2022 from IP address 130.238.189.191.

5. V. R. Stamenkovic, D. Strmcnik, P. P. Lopes, N. M. Markovic, Energy and fuels from electrochemical interfaces. *Nat. Mater.* **16**, 57–69 (2016).
6. M. K. Debe, Electrocatalyst approaches and challenges for automotive fuel cells. *Nature* **486**, 43–51 (2012).
7. G. T. Babcock, M. Wikström, Oxygen activation and the conservation of energy in cell respiration. *Nature* **356**, 301–309 (1992).
8. S. Ferguson-Miller, G. T. Babcock, Heme/copper terminal oxidases. *Chem. Rev.* **96**, 2889–2908 (1996).
9. P. J. Silva, Refining the reaction mechanism of O_2 towards its co-substrate in cofactor-free dioxygenases. *PeerJ* **4**, e2805 (2016).
10. L. Gabison *et al.*, X-ray, ESR, and quantum mechanics studies unravel a spin well in the cofactor-less urate oxidase. *Proteins* **79**, 1964–1976 (2011).
11. B. Minaev, Magnetic torque in superoxide ion is the main driving force of dioxygen activation in aerobic life. *Biomed. J. Sci. Tech. Res.* **38**, 30462–30472 (2021).
12. J. K. Nørskov, J. Rossmeisl, A. Logadottir, L. Lindqvist, Origin of the overpotential for oxygen reduction at a fuel-cell cathode. *J. Phys. Chem. B* **108**, 17886–17892 (2004).
13. Z. W. Seh *et al.*, Combining theory and experiment in electrocatalysis: Insights into materials design. *Science* **355**, eaad4998 (2017).
14. N. A. Kotov, L. M. Liz-Marzan, P. S. Weiss, Chiral nanostructures: New twists. *ACS Nano* **15**, 12457–12460 (2021).
15. J. R. Brandt, F. Salerno, M. J. Fuchter, The added value of small-molecule chirality in technological applications. *Nat. Rev. Chem.* **1**, 1–12 (2017).
16. R. Naaman, Y. Paltiel, D. Waldeck, Chiral molecules and the electron's spin. *Nat. Rev. Chem.* **3**, 250–260 (2019).
17. D. Mishra *et al.*, Spin-dependent electron transmission through bacteriorhodopsin embedded in purple membrane. *Proc. Natl. Acad. Sci. U.S.A.* **110**, 14872–14876 (2013).
18. S. Mishra, S. Pirbadian, A. K. Mondal, M. Y. El-Naggar, R. Naaman, Spin-dependent electron transport through bacterial cell surface multiheme electron conduits. *J. Am. Chem. Soc.* **141**, 19198–19202 (2019).
19. W. Mtangi, V. Kiran, C. Fontanesi, R. Naaman, The role of the electron spin polarization in water splitting. *J. Phys. Chem. Lett.* **6**, 4916–4922 (2015).
20. W. Mtangi *et al.*, Control of electrons' spin eliminates hydrogen peroxide formation during water splitting. *J. Am. Chem. Soc.* **139**, 2794–2798 (2017).
21. Y. Nie, L. Li, Z. Wei, Recent advancements in Pt and Pt-free catalysts for oxygen reduction reaction. *Chem. Soc. Rev.* **44**, 2168–2201 (2015).
22. S. Mishra *et al.*, Length-dependent electron spin polarization in oligopeptides and DNA. *J. Phys. Chem. C* **124**, 10776–10782 (2020).
23. M. Eckshtain-Levi *et al.*, Cold denaturation induces inversion of dipole and spin transfer in chiral peptide monolayers. *Nat. Commun.* **7**, 10744 (2016).
24. D. Wang *et al.*, Transition metal and nitrogen Co-doped carbon-based electrocatalysts for the oxygen reduction reaction: From active site insights to the rational design of precursors and structures. *ChemSusChem* **14**, 33–55 (2021).
25. X. Ge *et al.*, Oxygen reduction in alkaline media: From mechanisms to recent advances of catalysts. *ACS Catal.* **5**, 4643–4667 (2015).
26. A. J. Bard, L. R. Faulkner, *Electrochemical Methods: Fundamentals and Applications* (John Wiley & Sons, Inc., 2010).
27. T. Shinagawa, A. T. Garcia-Esparza, K. Takanabe, Insight on Tafel slopes from a microkinetic analysis of aqueous electrocatalysis for energy conversion. *Sci. Rep.* **5**, 13801 (2015).
28. S. L. Murov, I. Carmichael, G. L. Hug, *Handbook of Photochemistry* (Marcel Dekker, New York, ed. 2, 1993).
29. V. R. Stamenkovic *et al.*, Improved oxygen reduction activity on $Pt_3Ni(111)$ via increased surface site availability. *Science* **315**, 493–497 (2007).
30. M. Luo *et al.*, PdMo bimetallene for oxygen reduction catalysis. *Nature* **574**, 81–85 (2019).
31. R. Gao *et al.*, Pt/Fe_2O_3 with Pt–Fe pair sites as a catalyst for oxygen reduction with ultralow Pt loading. *Nat. Energy* **6**, 614–6236 (2021).
32. I. A. Rutkowska *et al.*, Activation of reduced-graphene-oxide supported Pt nanoparticles by aligning with WO_3-nanowires toward oxygen reduction in acid medium: Diagnosis with rotating-ring-disk voltammetry and double-potential-step chronocoulometry. *J. Electrochem. Soc.* **165**, J3384 (2018).
33. G. F. Wei, Y. H. Fang, Z. P. Liu, First principles Tafel kinetics for resolving key parameters in optimizing oxygen electrocatalytic reduction catalyst. *J. Phys. Chem. C* **116**, 12696–12705 (2012).
34. I. Meirzada *et al.*, Long-timescale magnetization ordering induced by an adsorbed chiral monolayer on ferromagnets. *ACS Nano* **15**, 5574–5579 (2021).
35. D. H. Waldeck, R. Naaman, Y. Paltiel, The spin selectivity effect in chiral materials. *APL Mater.* **9**, 040902 (2021).
36. J. Fransson, Vibrational origin of exchange splitting and chiral-induced spin selectivity. *Phys. Rev. B* **102**, 235416 (2020).
37. J. Fransson, Charge redistribution and spin polarization driven by correlation induced electron exchange in chiral molecules. *Nano Lett.* **21**, 3026–3032 (2021).
38. Z. Zeng *et al.*, Magnetic field-enhanced 4-electron pathway for well-aligned Co_3O_4/electrospun carbon nanofibers in the oxygen reduction reaction. *ChemSusChem* **11**, 580–588 (2018).
39. B. F. Minaev, Spin effects in reductive activation of O_2 by oxydase enzymes. *RIKEN Rev.* **44**, 147–149 (2002).
40. H. E. Lee *et al.*, Amino-acid- and peptide-directed synthesis of chiral plasmonic gold nanoparticles. *Nature* **556**, 360–365 (2018).
41. X. Yang, J. Nash, N. Oliveira, Y. Yan, B. Xu, Understanding the pH dependence of underpotential deposited hydrogen on platinum. *Angew. Chem. Int. Ed. Engl.* **58**, 17718–17723 (2019).
42. W. Xing, G. Yin, J. Zhang, *Rotating Electrode Methods and Oxygen Reduction Electrocatalysts* (Elsevier, 2014).
43. P. W. Atkins, *Molecular Quantum Mechanics* (Oxford University Press, ed. 2, 1983).

Downloaded from https://www.pnas.org by Uppsala Universitetsbibliotek on August 26, 2022 from IP address 130.238.189.191.